Biophysical Journal
Article

Biophysical Society

Motor Protein Accumulation on Antiparallel Microtubule Overlaps

Hui-Shun Kuan[1,2] and Meredith D. Betterton[1,*]
[1]Department of Physics and [2]Department of Chemistry and Biochemistry, University of Colorado at Boulder, Boulder, Colorado

ABSTRACT Biopolymers serve as one-dimensional tracks on which motor proteins move to perform their biological roles. Motor protein phenomena have inspired theoretical models of one-dimensional transport, crowding, and jamming. Experiments studying the motion of Xklp1 motors on reconstituted antiparallel microtubule overlaps demonstrated that motors recruited to the overlap walk toward the plus end of individual microtubules and frequently switch between filaments. We study a model of this system that couples the totally asymmetric simple exclusion process for motor motion with switches between antiparallel filaments and binding kinetics. We determine steady-state motor density profiles for fixed-length overlaps using exact and approximate solutions of the continuum differential equations and compare to kinetic Monte Carlo simulations. Overlap motor density profiles and motor trajectories resemble experimental measurements. The phase diagram of the model is similar to the single-filament case for low switching rate, while for high switching rate we find a new (to our knowledge) low density-high density-low density-high density phase. The overlap center region, far from the overlap ends, has a constant motor density as one would naïvely expect. However, rather than following a simple binding equilibrium, the center motor density depends on total overlap length, motor speed, and motor switching rate. The size of the crowded boundary layer near the overlap ends is also dependent on the overlap length and switching rate in addition to the motor speed and bulk concentration. The antiparallel microtubule overlap geometry may offer a previously unrecognized mechanism for biological regulation of protein concentration and consequent activity.

INTRODUCTION

The motion of motor proteins on biopolymers is important for diverse biological processes (1). Actin, microtubules, and nucleic acids can serve as one-dimensional tracks on which motor proteins (including myosins, kinesins, helicases, and ribosomes) move (2,3). Motors must accumulate on filaments in sufficient density to perform their biological roles. This motor accumulation along a biopolymer is affected by two key effects: directional walking of motors, and motor binding to/unbinding from the filament.

Motor accumulation on filaments is related to extensive theoretical work on asymmetric simple exclusion processes (ASEP) (4). In ASEP models, particles move on a one-dimensional lattice by biased hopping and experience excluded-volume interactions with other particles. These models have been applied to diverse examples of one-dimensional nonequilibrium transport ranging from molecular motors to vehicular and pedestrian traffic. Active particle motion leads to nonzero flux of particle density and nontrivial flux and density profiles. To compare to experimental studies of molecular motors, ASEP models have been extended to incorporate important biophysical ingredients such as binding kinetics. A model extending the totally asymmetric simple exclusion process (TASEP) to include motor binding and unbinding (Langmuir kinetics) predicted motor density profiles along single fixed-length filaments (5). Experimental work measured kinesin-8 motor protein traffic jams on microtubules and found good agreement with the predicted density profiles (6).

Motor motion on cytoskeletal filaments is important for biological length regulation, including regulation of the length of the polymer (7), lengths of overlap regions between filaments (8), and the length of cytoskeletal assemblies such as the mitotic spindle (9,10) and even whole cells (11,12). The case of regulation of microtubule (MT) length has seen the most work. MTs undergo nonequilibrium polymerization dynamics characterized by switching between distinct growing and shrinking states. While this dynamic instability alone leads to a broad distribution of MT lengths (13), numerous proteins targeted to MT ends modify their dynamics and can dramatically alter the length

Submitted September 25, 2015, and accepted for publication March 29, 2016.

*Correspondence: mdb@colorado.edu

Editor: Jennifer Ross.
http://dx.doi.org/10.1016/j.bpj.2016.03.039

distribution (14). Single MTs can have their length regulated, for example, by kinesin-8 motors that walk with directional bias and shorten the MT from its end (7,15,16). Theoretical work on TASEP-like models has described how length-dependent depolymerization affects otherwise static filaments (7,17,18), filaments with simplified polymerization kinetics (19–22), and dynamic MTs (23–25).

Because the mitotic spindle includes arrays of overlapping antiparallel MTs at the spindle midzone, regulation of MT overlaps is important for mitotic spindle function and cytokinesis. The MT crosslinking protein PRC1/Ase1/MAP65 and kinesin-4 motors (chromokinesins) play roles in maintenance of the spindle midzone in anaphase (26–28), along with other motors and MAPs (29). Direct binding interactions of PRC1 and kinesin 4 can cause length-dependent accumulation at plus ends of single MTs (30). Bieling et al. (8) reconstituted a minimal system of stable antiparallel MT overlaps in which PRC1 bound preferentially to overlapping regions of antiparallel MTs (8) (see also Subramanian et al. (31)). PRC1 recruited the kinesin-4 motor Xklp1 to the overlap. Xklp1 motors could bind to and unbind from the MTs, walk toward the plus end of each MT, and switch between the two MTs at a relatively high rate (8). Motors present near the MT plus ends slowed the polymerization speed, consistent with earlier work showing that Xklp1 inhibits dynamic instability (32) and affects spindle MT mass (33). As a result, antiparallel MT overlaps reached a constant length that depended on the bulk concentration of motors. This work demonstrated that motor-dependent regulation of dynamics and length can occur not just for single MTs, but also for overlapping MT pairs.

Here we model the density profiles of motor proteins on antiparallel MT overlaps of fixed lengths. We do not explicitly consider MT length regulation in this system, as the combination of binding kinetics and coupled switching of the motors between the two antiparallel filaments is sufficient to produce a rich phenomenology. Our work is an extension of the TASEP with binding kinetics on a single filament (5,34) to include two antiparallel filaments coupled by switching; it is also an extension of TASEP models of two antiparallel lanes with lane switching (35,36) to incorporate binding and unbinding kinetics.

We first develop the model and show that measured and estimated parameters can give overlap motor density profiles and motor trajectories qualitatively similar to those found in the experiments of Bieling et al. (8). We then develop an analytic solution to the mean-field steady-state equations, and use it to determine the phase diagram of the model. For high motor switching rate between filaments, we find a new (to our knowledge) low density-high density-low density-high density phase. We then study the model for the reference parameter set in more detail. Because the motor density profiles are controlled by both boundary conditions and a nonlocal total binding constraint, the density in the center of the overlap depends not just on motor binding kinetics but also on motor speed and overlap length. We find an analytical approximation that describes the overlap center density and the size of the motor-dense boundary layer near the overlap ends. The degree of motor accumulation near the overlap ends depends on the overlap length and motor switching rate in addition to the motor speed and bulk concentration. The coupling of motor motion, binding, and switching kinetics on antiparallel MT overlaps may therefore offer a previously unrecognized mechanism for the control of one-dimensional motor density profiles.

MATERIALS AND METHODS

Model

In this section, we develop a mathematical model of motor density on antiparallel filament overlaps, inspired by the experiments of Bieling et al. (8). In the experiments of Bieling et al. (8), the cross-linking protein PRC1 binds preferentially to overlapping regions of antiparallel MTs and recruits the kinesin motor protein Xklp1 to the overlap region. Because PRC1 and therefore the motors are present at much higher concentrations in the overlap, in the model we consider the overlap region only and model the regions of single filaments as sources or sinks of motor proteins (Fig. 1 *A*). While previous work has shown that PRC1/Ase1 alone can develop density inhomogeneities and exert forces on sliding MTs (37,38), in the experiments of Bieling et al. (8), little to no MT sliding occurred and the PRC1 distribution was uniform in the overlaps (8). Therefore we do not explicitly model the PRC1 molecules or their spatial distribution, but assume they are uniformly distributed so that each lattice site in the overlap is identical with a binding affinity that would correspond to the density-weighted average of the PRC1 and bare tubulin affinities. We treat each MT as a single track and neglect the multiple-protofilament structure of the MT, consistent with previous theoretical work (7,17–22,24). In our model, motors can bind to and unbind from each of the MTs, walk toward the plus end of a MT, and switch between the two MTs (Fig. 1 *A*).

There are two competing processes in this model: motor stepping (TASEP); and motor binding, unbinding, and MT switching (Langmuir kinetics). The Langmuir kinetics dominate the system behavior if the overlap length is sufficiently large, $N >> 1$, so that each bound motor can only walk for a short fraction of the overlap length before it unbinds. Thus, the competition between TASEP and Langmuir kinetics occurs only if the overall binding rate to one MT in the overlap $K_{on}c = Nk_{on}c$ (where c is the bulk motor concentration), and unbinding rate $K_{off} = Nk_{off}$, are of similar magnitude to the motor speed v (5).

In the next section, we develop the discrete microscopic model and corresponding stochastic simulation, then derive the mean-field continuum description.

Discrete model

We consider two overlapping antiparallel MTs of fixed length, so the number of sites N is fixed (Fig. 1 *A*). At each site, motor binding or unbinding can occur with binding rate $k_{on}c$, where k_{on} is the binding rate constant per site and c is the bulk motor concentration; the unbinding rate is k_{off}. Each bound motor steps at rate v to the next site toward the MT plus end (if the next site is unoccupied), and switches at rate s to the site on the adjacent MT (if that site is unoccupied). Note that Xklp1 is plus-end directed, and we therefore assume that the motion on a single MT is unidirectional.

The occupation number $\hat{n}_i$ is 1 if site i is occupied or 0 if site i is empty. Then the equations for interior sites ($2 < i < N - 1$) on MTs with plus ends to the right (R) and left (L) are

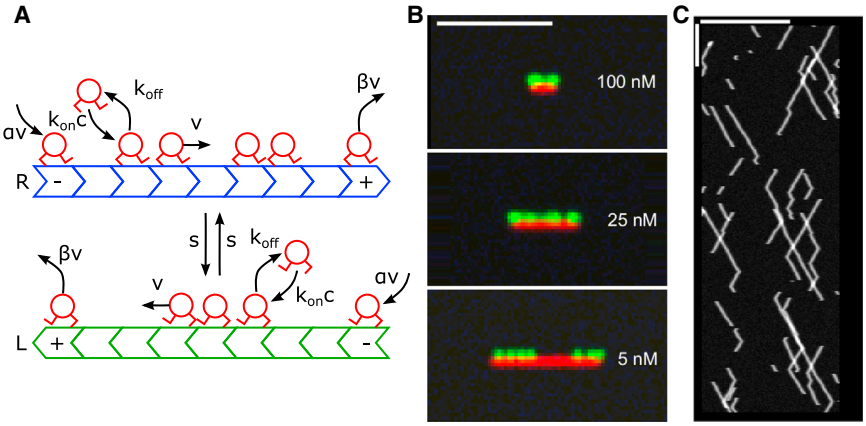

FIGURE 1 Model and results overview. (*A*) Schematic of the model of motor motion on an antiparallel microtubule overlap. Two filaments (*green* and *blue*) are modeled as one-dimensional lattices with their plus-ends oppositely oriented. The filaments are labled *R* (*L*) if the plus end is pointing to the right (*left*). Motors (*red*) bind to empty lattice sites with rate $k_{on}c$ and unbind with rate k_{off}. Bound motors step toward the MT plus-end with rate v (if the adjacent site toward the MT plus-end is empty) or switch to the other MT with rate s (if the corresponding site on the adjacent MT is empty). At MT minus ends, motors are inserted at rate αv. At MT plus ends, motors are removed at rate βv. (*B*) Simulated experimental images made from our kMC model. (*Green*) Motor density. (*Red*) Overlap region. Scale bar, 5 μm. Simulations used to generate these images used the reference parameter set (Table 1) and the indicated bulk motor concentrations. (*C*) Simulated kymograph made from our kMC model with motor spatial position on the horizontal axis and time increasing downwards. Horizontal scale bar, 10 μm. Vertical scale bar, 5 s. The simulations used to generate the kymograph used the reference parameter set and 0.5 nM bulk motor concentration. To see this figure in color, go online.

$$\frac{d\hat{n}_{R,i}(t)}{dt} = v\hat{n}_{R,i-1}(t)[1-\hat{n}_{R,i}(t)] - v\hat{n}_{R,i}(t)[1-\hat{n}_{R,i+1}(t)] + k_{on}c[1-\hat{n}_{R,i}(t)] - k_{off}\hat{n}_{R,i}(t) - s\hat{n}_{R,i}(t)[1-\hat{n}_{L,i}(t)] + s\hat{n}_{L,i}(t)[1-\hat{n}_{R,i}(t)], \quad (1)$$

$$\frac{d\hat{n}_{L,i}(t)}{dt} = v\hat{n}_{L,i+1}(t)[1-\hat{n}_{L,i}(t)] - v\hat{n}_{L,i}(t)[1-\hat{n}_{L,i-1}(t)] + k_{on}c[1-\hat{n}_{L,i}(t)] - k_{off}\hat{n}_{L,i}(t) - s\hat{n}_{L,i}(t)[1-\hat{n}_{R,i}(t)] + s\hat{n}_{R,i}(t)[1-\hat{n}_{L,i}(t)]. \quad (2)$$

At the boundary sites, we modify these equations to incorporate fluxes into and out of the overlap. The flux into the overlap is $v\alpha[1-\hat{n}_1(t)]$, where nonzero α results from motors moving into the overlap from the adjacent single-MT region. The flux out of the overlap is $v\beta\hat{n}_N(t)$, where β is derived from the rate at which motors at an MT plus-end unbind. In principle, each filament could have different boundary conditions. Because we have no physical reason to distinguish the two halves of the overlap, we focus on the symmetric case $\alpha_L = \alpha_R = \alpha$ and $\beta_L = \beta_R = \beta$. The resulting boundary site equations are

$$\frac{d\hat{n}_{R,1}(t)}{dt} = v\alpha[1-\hat{n}_{R,1}(t)] - v\hat{n}_{R,1}(t)[1-\hat{n}_{R,2}(t)], \quad (3)$$

$$\frac{d\hat{n}_{R,N}(t)}{dt} = v\hat{n}_{R,N-1}(t)[1-\hat{n}_{R,N}(t)] - v\beta\hat{n}_{R,N}(t), \quad (4)$$

$$\frac{d\hat{n}_{L,1}(t)}{dt} = v\hat{n}_{L,2}(t)[1-\hat{n}_{L,1}(t)] - v\beta\hat{n}_{L,1}(t), \quad (5)$$

$$\frac{d\hat{n}_{L,N}(t)}{dt} = v\alpha[1-\hat{n}_{L,N}(t)] - v\hat{n}_{L,N}(t)[1-\hat{n}_{L,N-1}(t)]. \quad (6)$$

As shown below, these boundary conditions fix the motor densities to be α at the minus-end and $1-\beta$ at the plus-end of each filament.

At steady state, we can derive a total binding constraint on the equations by summing all of the sites on both filaments. The bulk flux terms of the form $\hat{n}_{i-1}(t)[1-\hat{n}_i(t)]$ sum to zero and only the binding and boundary terms remain:

$$\sum_{i=2}^{N-1}\left[2k_{on}c - \left(k_{on}c + k_{off}\right)\left(\hat{n}_{R,i} + \hat{n}_{L,i}\right)\right] + v\alpha[2 - \hat{n}_{R,1}(t) - \hat{n}_{L,N}(t)] - v\beta[\hat{n}_{R,N}(t) + \hat{n}_{L,1}(t)] = 0. \quad (7)$$

We find a binding constraint on the total motor binding

$$\sum_{i=1}^{N}\hat{n}_{R,i}+\hat{n}_{L,i} = 2(\mathrm{N}-2)\frac{k_{on}c}{k_{on}c+k_{off}} + \frac{2v[\alpha(1-\alpha)-\beta(1-\beta)]}{k_{on}c+k_{off}} = 2(\mathrm{N}-2)\rho_0 + \frac{2v[\alpha(1-\alpha)-\beta(1-\beta)]}{k_{on}c+k_{off}}, \quad (8)$$

where we have defined the Langmuir density $\rho_0 = k_{on}c/(k_{on}c+k_{off})$. Therefore, at steady state, an equilibrium involving binding, unbinding, and the filament-end boundary conditions must be reached on average for the entire overlap. This is related to the zero-current condition found in previous work on the antiparallel TASEP without binding kinetics (35,36). We did not find an analytical solution to the discrete equations. Instead, we performed kinetic Monte Carlo (kMC) simulations of the discrete model (Supporting Material) and compared it to solutions in the continuum limit.

Mean-field continuum model

We derive the mean-field continuum model as in Parmeggiani et al. (5) by taking the stationary average $\langle\hat{n}_i\rangle \equiv \rho_i$, and applying the random phase approximation $\langle\hat{n}_i\hat{n}_{i+1}\rangle = \langle\hat{n}_i\rangle\langle\hat{n}_{i+1}\rangle$. We also assume motor commutation during track switching, $\langle\hat{n}_{R,i}\hat{n}_{L,i}\rangle = \langle\hat{n}_{L,i}\rangle\langle\hat{n}_{R,i}\rangle$, to give discrete mean-field equations with linear switching terms (Supporting Material). We take the continuum limit and nondimensionalize the parameters and variables by choosing the length of the overlap, L, as the unit of length and L/v as the unit of time. Capital letters denote the nondimensionalized parameters

($S = sL/v$ and so on; Supporting Material). We choose $x = 0$ as the center of the overlap, and the boundary conditions become $\rho_R(-0.5) = \rho_L(0.5) = \alpha$ and $\rho_R(0.5) = \rho_L(-0.5) = 1 - \beta$. The steady-state continuum mean-field equations are

$$0 = (2\rho_R - 1)\frac{\partial \rho_R}{\partial x} + K_{on}c(1-\rho_R) - K_{off}\rho_R - S\rho_R + S\rho_L, \tag{9}$$

$$0 = (1 - 2\rho_L)\frac{\partial \rho_L}{\partial x} + K_{on}c(1-\rho_L) - K_{off}\rho_L + S\rho_R - S\rho_L. \tag{10}$$

In the continuum mean-field model, the total binding constraint (Eq. 8) is

$$\begin{aligned}\int_{-1/2}^{1/2} dx\, \rho_R &= \int_{-1/2}^{1/2} dx\, \rho_L \\ &= \frac{K_{on}c}{K_{on}c + K_{off}} + \frac{\alpha(1-\alpha) - \beta(1-\beta)}{K_{on}c + K_{off}} \\ &= \rho_0 + \frac{\alpha(1-\alpha) - \beta(1-\beta)}{K_{on}c + K_{off}}.\end{aligned} \tag{11}$$

RESULTS

Motor density and trajectories in overlap

To study whether our model can qualitatively describe the motor density in antiparallel MT overlaps observed experimentally, we determined a reference parameter set corresponding to the experiments of Bieling et al. (8) (Table 1). Most parameters were directly measured by Bieling et al. We estimated the motor on rate constant k_{on} by comparison to the single-molecule imaging of low-density Xklp1 in an overlap (8). To estimate the minus-end boundary condition α, note that Bieling et al. found that Xklp1 binding was greatly increased on overlaps due to recruitment by PRC1. Low ionic strength (which favors motor-MT binding) was needed to observe significant Xklp1 binding to single MTs outside of overlaps. Therefore, we assume that the flux of motors into the overlap from outside is negligible, and set $\alpha = 0$ in our reference parameters. The plus-end boundary condition β is related to the motor unbinding rate at MT plus ends. While this end off-rate was not directly measured by Bieling et al. (8), kinesin motors typically pause at MT plus ends and have an end unbinding rate smaller than the unbinding rate in the bulk. We therefore expect that β lies between 0 (no end unbinding) and 2.7×10^{-3} (the value of β corresponding to an unbinding rate equal to k_{off}, the motor unbinding rate in the bulk). We found that $\beta = 2.7 \times 10^{-3}$ is so small that the motor density profiles were indistinguishable from those with $\beta = 0$ (Fig. S1 in the Supporting Material). Therefore we used $\beta = 0$ in our reference parameter set.

With these parameters, we studied kMC simulations of our model with varying motor concentration and overlap lengths corresponding to the steady-state values measured by Bieling et al. (8). We made simulated images that represent how our model's motor distributions would appear in an experiment with fluorescently tagged motors (*green*) and antiparallel MT overlap region (*red*; Fig. 1 *B*, and Supporting Material). Motors decorate the overlap, with greater density and end accumulation for higher bulk motor concentration. The simulated images are qualitatively similar to the experimental images (see Fig. 4 in Bieling et al. (8)). We also made simulated kymographs (Fig. 1 *C*, and Supporting Material), which show directed motor motion with direction reversal, qualitatively similar to the experimental results (see Figs. 6 and S5 in Bieling et al. (8)). We note that the experimental kymographs show a larger population of paused/immobile motors than occurs in our model.

Analytic solution of the steady-state continuum equations

To further study the behavior of our model, we determined analytic steady-state solutions of the continuum mean-field

TABLE 1 Parameter Values for the Reference Parameter Set

Symbol	Parameter	Reference Value	Notes
v	motor speed	0.5 μm s^{-1}	measured by Bieling et al. (8); varied up to 8 μm s^{-1} to study effect of varying speed on density profiles
k_{on}	binding rate constant	2.7×10^{-4} nM^{-1} s^{-1}	estimated based on motor density profiles and kymographs to give affinity of 6.3 nM, ~15× higher than measured for motor on single MT by Bieling et al. (42)
c	bulk motor concentration	1–200 nM	varied by Bieling et al. (8)
k_{off}	unbinding rate	0.169 s^{-1}	measured by Bieling et al. (8)
s	switching rate	0.44 s^{-1}	measured by Bieling et al. (8)
α	motor flux constant into overlap from MT minus end	0	motors bind primarily inside the overlap; see discussion in the Results; we varied α between 0 and 1 to determine the model phase diagram
β	motor flux constant out of overlap from MT plus end	0	an upper bound on the end motor unbinding rate is $\beta = 2.7 \times 10^{-3}$; see discussion in the Results; we varied β between 0 and 1 to determine the model phase diagram
N	number of sites	120–2500	varied to study overlaps of length 1–20 μm
δ	length of a single site	8 nm	length of an α-β tubulin dimer; see Bray (1)

equations. One solution to Eqs. 9 and 10 is the constant Langmuir density set by binding/unbinding equilibrium, $\rho_0 = K_{on}c/(K_{on}c + K_{off})$. To find spatially varying solutions, we first define $\sigma_{R,L} = \rho_{R,L} - 1/2$, the difference of the motor occupancies from $1/2$. The rate combinations are $k = K_{on}c + K_{off} + S$ and $\gamma = K_{on}c - K_{off}$. Then the equations become

$$\frac{d\sigma_R}{dx} = \frac{k}{2} - \frac{\gamma}{4\sigma_R} - \frac{S\sigma_L}{2\sigma_R} \tag{12}$$

$$\frac{d\sigma_L}{dx} = -\frac{k}{2} + \frac{\gamma}{4\sigma_L} + \frac{S\sigma_R}{2\sigma_L}. \tag{13}$$

Equations 12 and 13 are well defined for $\sigma_{R,L} \neq 0$. This allows solution of the differential equation relating $\sigma_R + \sigma_L$ and $\sigma_R - \sigma_L$ with one integration constant (Supporting Material). Our kMC simulation results for motor density in the overlap differ substantially from this analytic solution (Fig. S2), because the analytic solution (Eq. S18 in the Supporting Material) does not satisfy the total binding constraint (Eq. 11). Therefore, the full density profiles must be determined by matching continuum solutions corresponding to different integration constants. This mathematical result implies several remarkable properties of the density profiles, as discussed below.

Phase diagram

We determined the phase diagram of the model as a function of the boundary condition parameters α and β, as well as how the phase diagram changes with the other model parameters. We find four phases previously observed for the single-filament case (5), the low density (L), high density (H), low density-high density (LH), and Meissner (M) phases (Figs. 2 and S3). We distinguish two different classes of L, H, and LH phase on overlaps by whether they have a local maximum (labeled x) or a local minimum (labeled n) of the total motor density at the overlap center. In addition, for high switching rate, we observe a new (to our knowledge) low density-high density-low density-high density (LHLH) phase (Fig. 2).

We studied flows in the $\sigma_L - \sigma_R$ phase plane to determine the motor concentration profiles (Fig. S4) and therefore the phase diagram, as discussed in the Supporting Material and a followup article (39). Representative phase diagrams for small and large switching rates are shown in Fig. 3. We note that the new (to our knowledge) LHLH phase occurs when $\alpha < 0.5$ and the switching frequency is sufficiently high, conditions that could occur experimentally. This phase can appear for high switching rate when two analytic solutions to the steady-state continuum equations intersect, causing transition points in the phase plane where the density is ill defined (Figs. S4 and S5). Our LHLH phase is reminiscent of multiphase coexistence, as found by Pierobon et al. (40). However, in this previous work the multiphase coexistence occurs due to a point defect in the lane, while here it occurs for spatially uniform dynamics.

The phase boundaries change with parameters of the model. Increases (decreases) to the Langmuir density (through changes in bulk motor concentration or binding/unbinding rate constants) shift the lower boundary of the LH phase closer to (farther from) the line where $1 - \beta = 0.5$ when $\alpha > \rho_0$ and closer to (farther from) the line $\alpha = \beta$ when $\alpha < \rho_0$. Similar shifts occur for the upper boundary of the LH phase. The motor speed affects the width and the shape of the LH phase: for higher motor

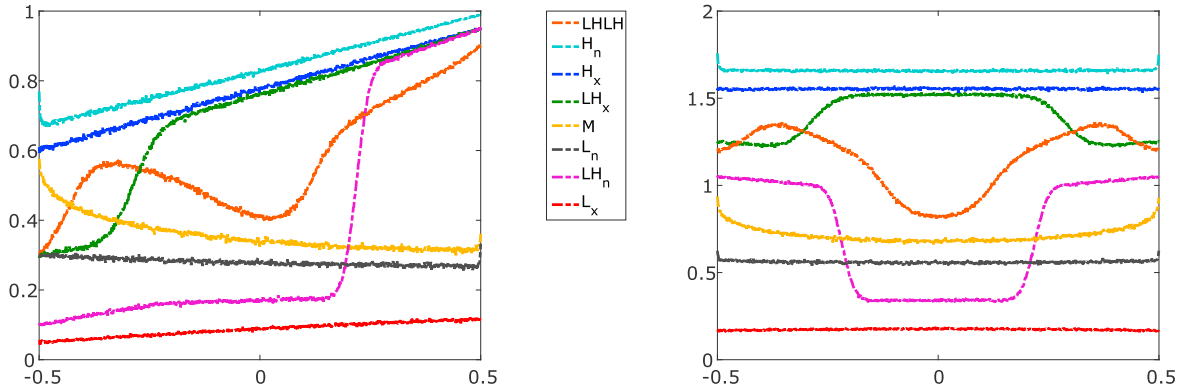

FIGURE 2 Nonequilibrium phases. (*Left*) Motor density $\rho_R(x)$ on MT with rightward-moving motors. (*Right*) Total motor density $\rho_R(x) + \rho_L(x)$ on both MTs in the overlap. The parameters comprise the reference parameter set of Table 1 with a bulk motor concentration of 200 nM, except for the switching rates, which are 0.5 s^{-1} for the LHLH curve and 0.1 s^{-1} for all other curves and the boundary conditions, as noted below. (*LHLH*) low density-high density-low density-high density coexistence ($\alpha = 0.3$, $\beta = 0.9$, *orange*). (H_n) High-density center-minimum phase ($\alpha = 0.95$, $\beta = 0.99$, *light blue*). (H_x) High-density center-maximum phase ($\alpha = 0.6$, $\beta = 0.95$, *dark blue*). (LH_x) Low-density/high-density center-maximum coexistence ($\alpha = 0.3$, $\beta = 0.95$, *green*). (*M*) Meissner phase $\alpha = 0.6$, $\beta = 0.4$, *yellow*). (L_n) Low-density center-minimum phase ($\alpha = 0.3$, $\beta = 0.4$, *black*). (LH_n) Low-density/high-density center-minimum coexistence ($\alpha = 0.1$, $\beta = 0.95$, *magenta*). (L_x) Low-density center-maximum phase ($\alpha = 0.05$, $\beta = 0.1$, *red*). To see this figure in color, go online.

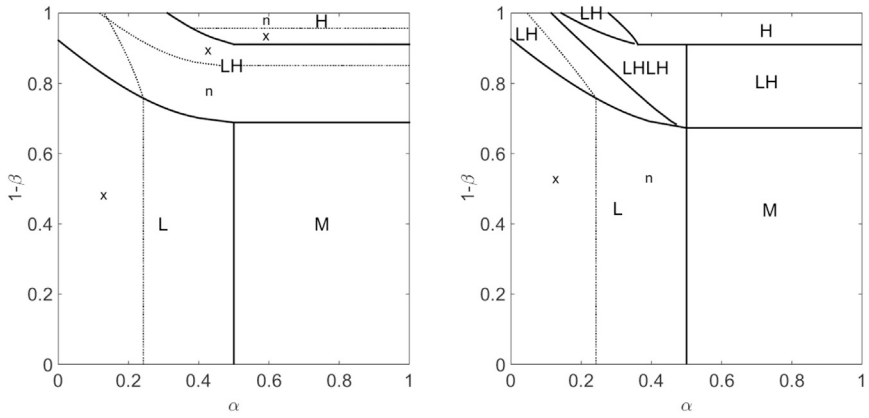

FIGURE 3 Phase diagrams. (*Left*) Low switching rate (0.1 s^{-1}); (*right*) high switching rate (0.5 s^{-1}). Solid lines indicate phase boundaries, and dotted lines indicate boundaries between center-maximum (x) and center-minimum (n) overlap motor density profiles. The bulk motor concentration is 200 nM, the motor speed is 5 $\mu m\ s^{-1}$, and other parameters are the reference values (Table 1).

speed, the LH phase region becomes narrower in width and the LH boundaries become more flat.

Density profiles for reference parameters

The motor density profiles that we determine by kMC simulation are qualitatively consistent with those observed experimentally (Figs. 1 and 4). Here we illustrate our results for the reference parameter set (Table 1); in the Supporting Material we also discuss a large-S parameter set chosen to approximate the limit of large switching rate (Table S1; Fig. S6). This parameter regime typically shows the LH phase, where the density profiles have three regions separated by domain walls. For motors moving to the right, there is a boundary layer on the left with the motor density increasing from zero, then a region of approximately linearly varying density, then a sharp transition to another boundary layer of linearly increasing density that approaches 1 on the right boundary (Fig. 4). If we fix all other parameters, the boundary layer regions increase in size as the bulk motor concentration increases. The total motor density in the overlap is the sum of the motor densities on the two filaments, which have the symmetry $\rho_L(-x) = \rho_R(x)$. The linear density variation near the overlap ends can be seen in the continuum mean-field equations (Supporting Material): the slope is $K_{on}c + S$ at the minus end and $K_{off} + S$ at the plus end. This approximation agrees well with simulation results near the overlap ends (Figs. S2 and S7).

Control of center density by the total binding constraint

Motor density profiles must satisfy the total binding constraint of Eq. 11, which requires that when $\alpha = \beta = 0$, the integral of the density on a single MT must equal ρ_0, the Langmuir density determined by binding/unbinding equilibrium. We verified that the total binding constraint is satisfied in our simulations by determining the integrated motor density and comparing it to ρ_0 (Fig. S8). However, as noted above, the analytic solutions we found for the steady-state motor density (Eqs. S18, S23, and S24) do not in general satisfy the total binding constraint. As a result, the motor concentration in the center of the filaments does not necessarily approach the Langmuir density $\rho_0 = K_{on}c/(K_{on}c + K_{off})$ (Fig. 4). This is a significant difference between the model of microtubule overlaps we study and the single-filament model (5).

The total binding constraint also controls the length of the boundary layer regions near the overlap ends. To derive an analytic approximation for this length, we approximate the motor densities as piecewise linear, and assume the

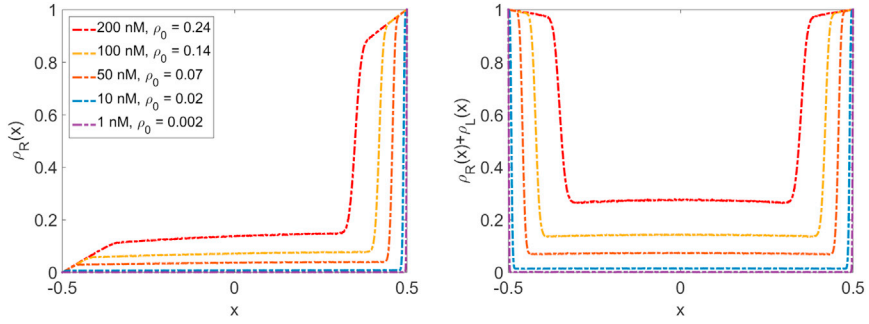

FIGURE 4 Motor density profiles for the reference parameter set. (*Left*) Motor density $\rho_R(x)$ on MT with rightward-moving motors. (*Right*) Total motor density $\rho_R(x) + \rho_L(x)$ on both MTs in the overlap. Parameters comprise the reference parameter set of Table 1 with the bulk motor concentrations indicated in the legend. To see this figure in color, go online.

domain walls are infinitely thin so that we can neglect them in integrating the concentration (Fig. S9). A filament is divided into three regions: boundary layers near the plus- and minus-ends (x_{bl}) and the central region. We can then determine the motor density profile (Eq. S28), the boundary layer ends (Eq. S30), and the motor density in the center of the overlap, ρ_c (Eq. S31).

The motor density at the center of the overlap is $\rho_c \neq \rho_0$, even when the overlap is long. Instead, the center density depends on the motor speed and filament switching rate in addition to binding parameters (Fig. 4). In Fig. 5, we compare simulation results and the prediction of Eq. S31, showing that our approximation is in good agreement with simulations. (Note that our approximation of the density as linearly varying becomes less exact for slow motor speeds, leading to a discrepancy between simulation results and our analytic approximation.) For comparison, we show the Langmuir density ρ_0 for the same parameters. Varying motor speed has no effect on ρ_0 (*right panel*), but a significant effect on ρ_c. To further illustrate the dependence of the center density on motor kinetic parameters, we show in Fig. 6 examples of motor density profiles from kMC simulations with varying motor speed. Changing motor kinetic parameters can have a large effect on the center density in the overlap, even for systems with identical binding kinetic parameters and ρ_0.

Control of end accumulation by the total binding constraint

The length of the boundary layer at the overlap ends depends on motor binding and kinetic parameters as well as the overlap length (Eq. S30). We compared the analytic approximation to simulation results and found good agreement (Fig. S10), allowing us to predict how varying experimental control parameters will alter the degree of motor accumulation near the overlap ends (Fig. 7). We note that although the boundary layer lengths predicted for typical experimental parameters are below the optical resolution limit of $\approx$250 nm, they could be distinguished by fits of fluorescent motor intensity profiles to model predictions (compare to Figs. 1, 4, and 6), similar to how fits to a Gaussian fluorescence intensity profile allow subresolution localization of single molecules (41).

The total binding constraint means the boundary layer length is determined as fraction of the overlap length. In the single-filament model, the motor density profile in the MT minus-end boundary layer is independent of MT length (17,24), with important consequences: MT length regulation by the kinesin-8 motor Kip3 (7,16) depends on a motor density profile that maintains the same functional form near the minus end as MT length changes. By contrast, on antiparallel MT overlaps, the density profile, boundary-layer length, and extent of motor accumulation at the overlap-ends change with overlap length (Fig. 7). This means that a length-regulation mechanism identical to that of Kip3 cannot occur on antiparallel MT overlaps.

CONCLUSIONS

We studied a model of motor motion on antiparallel MT overlaps that incorporates motor binding and unbinding, plus-end directed motor motion, and switching between filaments (Fig. 1). Our model is inspired by the experiments of Bieling et al. (8) on the motion of the kinesin-4 motor Xklp1 on antiparallel MT overlaps. Our model is an extension of previous theory that studied motor motion on a single MT with binding kinetics (5,34), or motor motion on two antiparallel filaments with lane switching, but no binding kinetics (35,36). To our knowledge, this is the first theoretical study of a two-lane TASEP model with oppositely oriented lanes, switching, and binding/unbinding.

To compare to the experiments of Bieling et al. (8), we used measured or estimated parameters (Table 1). Because PRC1 recruits motors directly into the overlap and motor binding to single MTs is much weaker, we neglect motor binding to MTs outside of the overlap and set the minus-end flux parameter $\alpha = 0$. Using the bulk motor unbinding rate K_{off} as an upper bound on the plus-end unbinding rate, we find $\beta \leq 2.7 \times 10^{-3}$. This value is sufficiently small that it gives motor density profiles indistinguishable from those with $\beta = 0$ (Fig. S1). Therefore no-flux boundary conditions with $\alpha = \beta = 0$ are used to model the experiments. Simulated images of the motor distribution in an overlap and simulated kymographs of motor trajectories are similar to those found experimentally (Fig. 1).

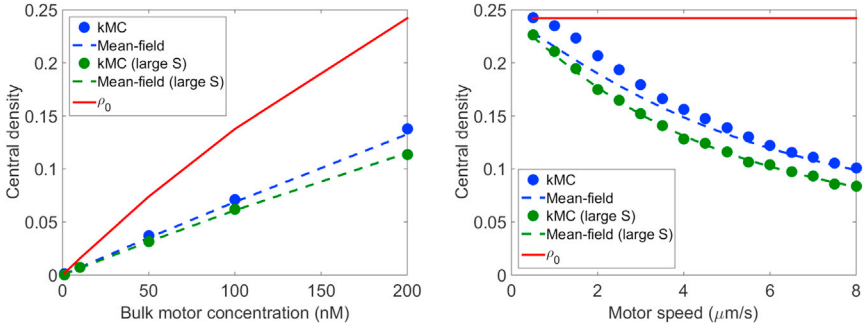

FIGURE 5 Motor density at the center of the overlap. (*Left*) Variation with bulk motor concentration; (*right*) variation with motor speed. Points indicate simulation results and dashed lines theoretical prediction from Eq. S31. The red line shows the value of the Langmuir density ρ_0 for the same parameters. To see this figure in color, go online.

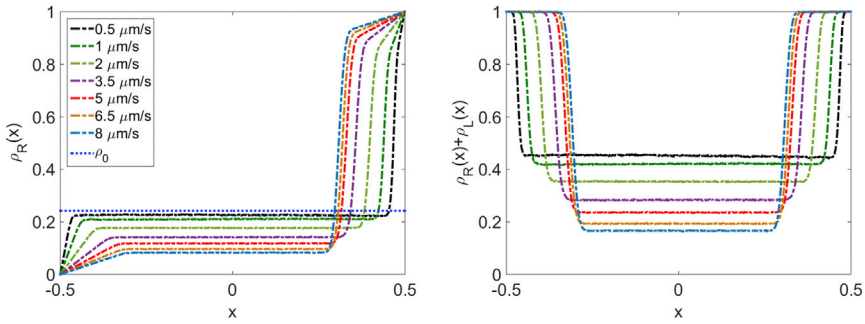

FIGURE 6 Dependence of density profiles on motor speed. (*Left*) Motor density $\rho_R(x)$ on MT with rightward-moving motors. (*Right*) Total motor density $\rho_R(x) + \rho_L(x)$ on both MTs in the overlap. Varying motor speed can significantly alter the motor density at the center of the overlap. These simulations use the large-S parameter set of Table S1 with bulk motor concentration $c = 200$ nM and the motor speeds indicated in the legend. To see this figure in color, go online.

We derived analytical and approximate solutions of the continuum steady-state equations and compared them to kMC simulation results (Fig. S2). Focusing on the symmetric case where the boundary conditions α and β are the same for both filaments in the overlap, we used both kMC simulations and phase plane flows (Figs. S3–S5) to determine the nonequilibrium phases possible in our model (Fig. 2). For low rate of motor switching between filaments in the overlap, we find the low-density, high-density, low-density/high-density, and Meissner phases previously studied for the single-lane case (5). In addition, for high switching rate we find a novel (to our knowledge) low density-high density-low density-high density phase with three domain walls. We determined representative phase diagrams for small and large switching rates (Fig. 3). We discuss determination of the phase diagram in more detail in a longer follow-up article (39).

We then studied the model in more detail both for the reference parameters and a high-switching-rate parameter set (Table S1). Results of kMC simulations (Figs. 4 and S6) agree well with exact and approximate solutions of the continuum steady-state equations (Figs. S2 and S7). In contrast to systems in which motors move on single filaments (7,17–22,24), we find that antiparallel overlaps with no-flux boundary conditions have zero total current. This leads to a total binding constraint that the integral of the total motor density on a single filament must equal ρ_0, the motor density set by binding/unbinding equilibrium (Fig. S8).

For the experimentally relevant low-density/high-density coexistence phase, the density profiles are approximately piecewise linear (Fig. S9). This motivates an analytic approximation to determine the density profiles consistent with the total binding constraint and gives analytic expressions for the overlap center motor density and the length of the boundary layer in which motors accumulate near the overlap ends. We find that as a result of the total binding constraint, the motor density at the center of the overlap is not determined solely by the motor binding equilibrium, but is also controlled by the overlap length, motor speed, and filament switching rate (Figs. 5 and 6). These same parameters control the length of the boundary layer at the overlap ends where motors accumulate (Fig. S10).

The mitotic spindle contains arrays of overlapping antiparallel MTs to which multiple motors and cross linkers bind (29). The surprising differences in motor density profiles between single filaments and the antiparallel overlaps we study here are therefore of interest in the study of the spindle midzone. For antiparallel overlaps, both the motor density far from the overlap ends and the number of motors near the overlap ends can be tuned not just by motor binding kinetics but also by motor speed, filament switching rate, and overlap length (Fig. 7). The antiparallel filament geometry gives biological systems additional handles to control motor density, its spatial distribution, and therefore motor function. Motor density can affect recruitment of other proteins and MT dynamics. Therefore, this previously undescribed mechanism of regulation of motor density along MTs may offer advantages to the control of motor activity.

For single MTs, length regulation by the kinesin-8 motor Kip3 depends on a functional form of motor density that is independent of MT length (7,16). The physics we describe here means that the motor density and extent of motor

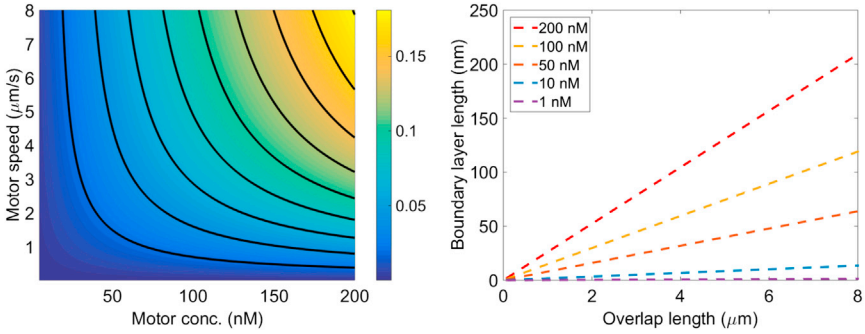

FIGURE 7 Control of boundary layer length. (*Left*) Boundary layer length as a fraction of total overlap length, shown as a function of bulk motor concentration and motor speed. (*Right*) Boundary layer length as a function of overlap length for the reference parameter set and varying bulk motor concentration. The boundary layer length is the distance at each end of the overlap where significant motor accumulation occurs and is determined by Eq. S30. To see this figure in color, go online.

accumulation at the overlap ends depends on overlap length. Therefore, length regulation of antiparallel MT overlaps must occur differently. In future work, it will be of interest to understand how the motor density profiles on fixed-length overlaps can be used to understand the length regulation of dynamic overlaps.

SUPPORTING MATERIAL

Supporting Materials and Methods, ten figures, and one table are available at http://www.biophysj.org/biophysj/supplemental/S0006-3495(16)30153-9.

AUTHOR CONTRIBUTIONS

H.-S.K. and M.D.B. designed research, performed research, contributed analytic tools, analyzed data, and wrote the article.

ACKNOWLEDGMENTS

We thank Robert Blackwell, Matthew Glaser, and Loren Hough for useful discussions.

This work was supported by National Science Foundation grant No. DMR-0847685 and National Institutes of Health No. K25 GM110486 to M.D.B., a fellowship to H.-S.K. provided by matching funds from the National Institutes of Health/University of Colorado Biophysics Training Program, and facilities of the Soft Materials Research Center under the National Science Foundation Materials Research Science and Engineering Centers grants No. DMR-0820579 and No. DMR-1420736. This worked used code from the Danuser and Jaqaman labs, provided through the Computational Image Analysis in Cellular and Developmental Biology course at MBL, and funded by National Institutes of Health No. R25 GM103792.

REFERENCES

1. Bray, D. 2000. Cell Movements: from Molecules to Motility. Routledge, New York.
2. Kolomeisky, A. B. 2015. Motor Proteins and Molecular Motors. CRC Press, Boca Raton, FL.
3. Chowdhury, D. 2013. Modeling stochastic kinetics of molecular machines at multiple levels: from molecules to modules. *Biophys. J.* 104:2331–2341.
4. Helbing, D. 2001. Traffic and related self-driven many-particle systems. *Rev. Mod. Phys.* 73:1067–1141.
5. Parmeggiani, A., T. Franosch, and E. Frey. 2004. Totally asymmetric simple exclusion process with Langmuir kinetics. *Phys. Rev. E Stat. Nonlin. Soft Matter Phys.* 70:046101.
6. Leduc, C., K. Padberg-Gehle, …, J. Howard. 2012. Molecular crowding creates traffic jams of kinesin motors on microtubules. *Proc. Natl. Acad. Sci. USA.* 109:6100–6105.
7. Varga, V., C. Leduc, …, J. Howard. 2009. Kinesin-8 motors act cooperatively to mediate length-dependent microtubule depolymerization. *Cell.* 138:1174–1183.
8. Bieling, P., I. A. Telley, and T. Surrey. 2010. A minimal midzone protein module controls formation and length of antiparallel microtubule overlaps. *Cell.* 142:420–432.
9. Goshima, G., R. Wollman, …, R. D. Vale. 2005. Length control of the metaphase spindle. *Curr. Biol.* 15:1979–1988.
10. Walczak, C. E., T. J. Mitchison, and A. Desai. 1996. XKCM1: a *Xenopus* kinesin-related protein that regulates microtubule dynamics during mitotic spindle assembly. *Cell.* 84:37–47.
11. Rivero, F., B. Köppel, …, A. A. Noegel. 1996. The role of the cortical cytoskeleton: F-actin crosslinking proteins protect against osmotic stress, ensure cell size, cell shape and motility, and contribute to phagocytosis and development. *J. Cell Sci.* 109:2679–2691.
12. Revenu, C., R. Athman, …, D. Louvard. 2004. The co-workers of actin filaments: from cell structures to signals. *Nat. Rev. Mol. Cell Biol.* 5:635–646.
13. Dogterom, M., and S. Leibler. 1993. Physical aspects of the growth and regulation of microtubule structures. *Phys. Rev. Lett.* 70:1347–1350.
14. Drummond, D. R. 2011. Regulation of microtubule dynamics by kinesins. *Semin. Cell Dev. Biol.* 22:927–934.
15. Gupta, M. L., Jr., P. Carvalho, …, D. Pellman. 2006. Plus end-specific depolymerase activity of Kip3, a kinesin-8 protein, explains its role in positioning the yeast mitotic spindle. *Nat. Cell Biol.* 8:913–923.
16. Varga, V., J. Helenius, …, J. Howard. 2006. Yeast kinesin-8 depolymerizes microtubules in a length-dependent manner. *Nat. Cell Biol.* 8:957–962.
17. Hough, L. E., A. Schwabe, …, M. D. Betterton. 2009. Microtubule depolymerization by the Kinesin-8 motor Kip3p: a mathematical model. *Biophys. J.* 96:3050–3064.
18. Reese, L., A. Melbinger, and E. Frey. 2011. Crowding of molecular motors determines microtubule depolymerization. *Biophys. J.* 101:2190–2200.
19. Govindan, B. S., M. Gopalakrishnan, and D. Chowdhury. 2008. Length control of microtubules by depolymerizing motor proteins. *Europhys. Lett.* 83:40006.
20. Johann, D., C. Erlenkämper, and K. Kruse. 2012. Length regulation of active biopolymers by molecular motors. *Phys. Rev. Lett.* 108:258103.
21. Melbinger, A., L. Reese, and E. Frey. 2012. Microtubule length regulation by molecular motors. *Phys. Rev. Lett.* 108:258104.
22. Reese, L., A. Melbinger, and E. Frey. 2014. Molecular mechanisms for microtubule length regulation by kinesin-8 and XMAP215 proteins. *Interface Focus.* 4:20140031.
23. Tischer, C., P. R. Ten Wolde, and M. Dogterom. 2010. Providing positional information with active transport on dynamic microtubules. *Biophys. J.* 99:726–735.
24. Kuan, H.-S., and M. D. Betterton. 2013. Biophysics of filament length regulation by molecular motors. *Phys. Biol.* 10:036004.
25. Glunčić, M., N. Maghelli, …, I. M. Tolić. 2015. Kinesin-8 motors improve nuclear centering by promoting microtubule catastrophe. *Phys. Rev. Lett.* 114:078103.
26. Kurasawa, Y., W. C. Earnshaw, …, K. Todokoro. 2004. Essential roles of KIF4 and its binding partner PRC1 in organized central spindle midzone formation. *EMBO J.* 23:3237–3248.
27. Zhu, C., and W. Jiang. 2005. Cell cycle-dependent translocation of PRC1 on the spindle by Kif4 is essential for midzone formation and cytokinesis. *Proc. Natl. Acad. Sci. USA.* 102:343–348.
28. Khmelinskii, A., C. Lawrence, …, E. Schiebel. 2007. Cdc14-regulated midzone assembly controls anaphase B. *J. Cell Biol.* 177:981–993.
29. Fededa, J. P., and D. W. Gerlich. 2012. Molecular control of animal cell cytokinesis. *Nat. Cell Biol.* 14:440–447.
30. Subramanian, R., S.-C. Ti, …, T. M. Kapoor. 2013. Marking and measuring single microtubules by PRC1 and kinesin-4. *Cell.* 154:377–390.
31. Subramanian, R., E. M. Wilson-Kubalek, …, T. M. Kapoor. 2010. Insights into antiparallel microtubule crosslinking by PRC1, a conserved nonmotor microtubule binding protein. *Cell.* 142:433–443.
32. Bringmann, H., G. Skiniotis, …, T. Surrey. 2004. A kinesin-like motor inhibits microtubule dynamic instability. *Science.* 303:1519–1522.
33. Castoldi, M., and I. Vernos. 2006. Chromokinesin Xklp1 contributes to the regulation of microtubule density and organization during spindle assembly. *Mol. Biol. Cell.* 17:1451–1460.
34. Parmeggiani, A., T. Franosch, and E. Frey. 2003. Phase coexistence in driven one-dimensional transport. *Phys. Rev. Lett.* 90:086601.

35. Juhász, R. 2007. Weakly coupled, antiparallel, totally asymmetric simple exclusion processes. *Phys. Rev. E Stat. Nonlin. Soft Matter Phys.* 76:021117.

36. Ashwin, P., C. Lin, and G. Steinberg. 2010. Queueing induced by bidirectional motor motion near the end of a microtubule. *Phys. Rev. E Stat. Nonlin. Soft Matter Phys.* 82:051907.

37. Braun, M., Z. Lansky, …, M. E. Janson. 2011. Adaptive braking by Ase1 prevents overlapping microtubules from sliding completely apart. *Nat. Cell Biol.* 13:1259–1264.

38. Lansky, Z., M. Braun, …, S. Diez. 2015. Diffusible crosslinkers generate directed forces in microtubule networks. *Cell.* 160:1159–1168.

39. Kuan, H.-S., and M. D. Betterton. 2016. Phase-plane analysis of the totally asymmetric simple exclusion process with binding kinetics and switching between antiparallel lanes. *ArXiv:1604.00690 [physics.bio-ph] 7 March 2016.*

40. Pierobon, P., M. Mobilia, …, E. Frey. 2006. Bottleneck-induced transitions in a minimal model for intracellular transport. *Phys. Rev. E Stat. Nonlin. Soft Matter Phys.* 74:031906.

41. Yildiz, A., J. N. Forkey, …, P. R. Selvin. 2003. Myosin V walks hand-over-hand: single fluorophore imaging with 1.5-nm localization. *Science.* 300:2061–2065.

42. Bieling, P., I. Kronja, and T. Surrey. 2010. Microtubule motility on reconstituted meiotic chromatin. *Curr. Biol.* 20:763–769.

Biophysical Journal, Volume *110*

Supplemental Information

Motor Protein Accumulation on Antiparallel Microtubule Overlaps

Hui-Shun Kuan and Meredith D. Betterton

Supporting Material

H.-S. Kuan and M. D. Betterton
(Dated: April 27, 2016)

I. KINETIC MONTE CARLO SIMULATIONS

We performed kinetic Monte Carlo (kMC) simulations of the discrete model with time step Δt and the following rules at each time step for an overlap with $2N$ sites:

1. Randomly choose a filament (R/L) and site i.

2. If the site is empty, attach a motor with probability $k_{\text{on}}c\Delta t$. If the site is occupied, detach the motor with probability $k_{\text{off}}\Delta t$.

3. If the site is occupied and the adjacent site toward the MT plus end is empty, move the motor forward with probability $v\Delta t$.

4. If the site is occupied and the corresponding site on the neighboring MT is empty, switch the motor to the other filament with probability $s\Delta t$.

5. Enforce the boundary conditions: site 1 on filament R and site N on filament L are occupied with probability α, while site N on filament R and site 1 on filament L are occupied with probability $(1-\beta)$.

6. Repeat steps 1-5 $2N$ times total to sample all sites on both MTs.

We typically choose $\Delta t = 5 \times 10^{-4}$ s such that the characteristic time for motor binding/unbinding is about 10^5 time steps, if the bulk motor concentration is 200 nM. To reach steady state we run for 4×10^7 time steps, and then collect data in a measurement run of 2×10^7 time steps. The average motor concentration is obtained by averaging 10^4-10^5 samples, separated by 200 time steps. For simulations of the large-S parameter set, we choose $\Delta t = 5 \times 10^{-6}$ s such that the characteristic time for motor binding/unbinding is about 10^7 steps if the bulk motor concentration is 200 nM.

A. Simulated images

The simulated images of motor density profiles shown in fig. 1B in the main text were created by running kMC simulations with 100 nM bulk motor concentration on a 120-site overlap (0.96 μm long), 25 nM bulk motor concentration on a 360-site overlap (2.88 μm long), and 5 nM bulk motor concentration on a 600-site overlap (4.8 μm long). After the simulation reached steady state, we created the images by sampling the motor density. In the green channel, we approximated a 100-ms experimental exposure by summing instantaneous density profiles from 20 consecutive 0.005 s simulation snapshots. Each motor simulated image produced a Gaussian intensity profile with a standard deviation of 150 nM. The intensity profiles were binned into 150-nm wide simulated pixels. We then added a constant background intensity level and Gaussian noise to each pixel. In the red channel, the overlap was defined by a Gaussian line of constant intensity, with background and noise added. The green and red simulated channels were offset by 2 pixels to simulate chromatic

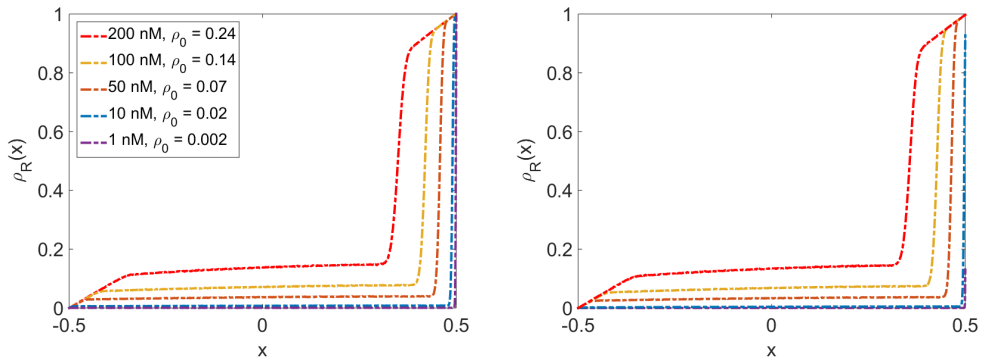

FIG. S1. Comparison of motor density profiles for zero and small β. Left: motor density $\rho_R(x)$ for $\beta = 0$. Right: motor density $\rho_R(x)$ for $\beta = 2.7 \times 10^{-3}$. Other parameters are the reference parameters with motor concentrations as shown in the legend.

aberration. In the blue channel, only background and Gaussian noise were present. The images from each motor concentration were brightness and contrast adjusted.

The simulated motor kymographs shown in fig. 1C in the main text were made by sampling a kMC simulation performed at 0.5 nM bulk motor concentration on a 2500-site overlap (20 μm long). The motor density was sampled every 0.025 s over a 50 s simulation, and the kymograph was constructed from the central 2000 sites of the overlap. Each motor in the simulated kymograph produced a Gaussian intensity profile with a standard deviation of 150 nM. The intensity profiles were binned into 150-nm wide simulated pixels. We then added a constant background intensity level and Gaussian pixel noise. The kymograph was brightness and contrast adjusted.

B. Comparison of zero and small β

In fig. S1 we show simulation results for the reference parameter set for filament flux plus-end boundary conditions with $\beta = 0$ and $\beta = 2.7 \times 10^{-3}$. The density profiles are nearly identical.

II. MEAN-FIELD CONTINUUM MODEL

To derive the mean-field continuum model, we first take the stationary average $\langle \hat{n}_i \rangle \equiv \rho_i$, apply the random phase approximation, $\langle \hat{n}_i \hat{n}_{i+1} \rangle = \langle \hat{n}_i \rangle \langle \hat{n}_{i+1} \rangle$, and assume motor commutation during track switching $\langle \hat{n}_{R,i} \hat{n}_{L,i} \rangle = \langle \hat{n}_{L,i} \rangle \langle \hat{n}_{R,i} \rangle$. The resulting discrete equations in the bulk are

$$\frac{\partial \rho_{R,i}}{\partial t} = -v\rho_{R,i}(1-\rho_{R,i+1}) + v\rho_{R,i-1}(1-\rho_{R,i}) + k_{\text{on}}c(1-\rho_{R,i}) - k_{\text{off}}\rho_{R,i} - s\rho_{R,i} + s\rho_{L,i} \quad \text{(S1)}$$

$$\frac{\partial \rho_{L,i}}{\partial t} = -v\rho_{L,i}(1-\rho_{L,i-1}) + v\rho_{L,i+1}(1-\rho_{L,i}) + k_{\text{on}}c(1-\rho_{L,i}) - k_{\text{off}}\rho_{L,i} - s\rho_{L,i} + s\rho_{R,i} \quad \text{(S2)}$$

and for the boundaries:

$$\frac{\partial \rho_{R,1}}{\partial t} = v\alpha(1-\rho_{R,1}) - v\rho_{R,1}(1-\rho_{R,2}), \quad \text{(S3)}$$

$$\frac{\partial \rho_{R,N}}{\partial t} = -v\beta\rho_{R,N} + v\rho_{R,N-1}(1-\rho_{R,N}), \quad \text{(S4)}$$

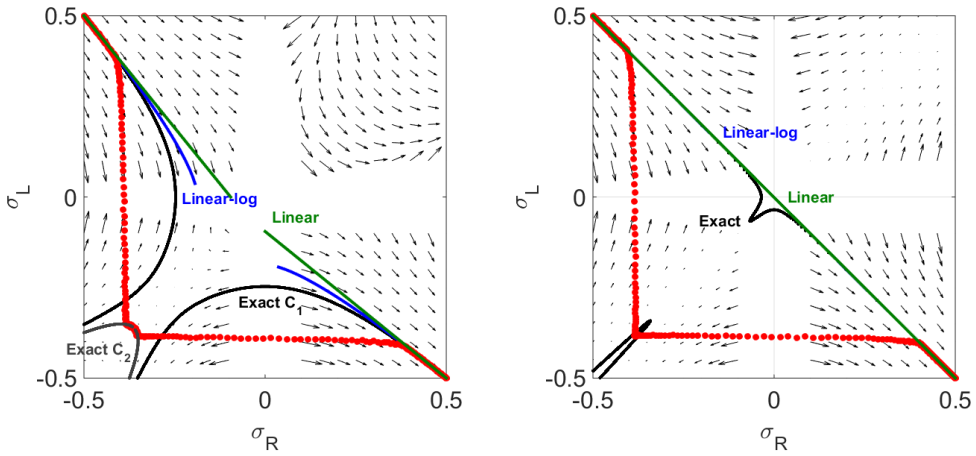

FIG. S2. Phase portraits in the σ_R-σ_L plane. Left: experimental parameter set; right: large-S parameter set. Both use a bulk motor concentration of 200 nM. The arrows indicate the direction of change of the densities as determined by Eqns. S9, S10. Black lines are the exact solutions to the continuum equations (Eqn. S18), red dots are simulation results, green line is the linear approximate solution near the ends of the overlap (Eqns. S19, S20), and blue line is the linear-log approximate solution near the ends of the overlap (Eqns. S23, S24).

and similarly for L.

We take the continuum limit where ρ_i becomes a continuous field $\rho(x)$, and define $\rho_{i\pm1} \to \rho(x \pm \delta)$, where δ is a length per motor binding site on the MT. We Taylor expand $\rho(x \pm \delta)$ to second order and nondimensionalize the parameters and variables by choosing the length of the MT, L, as the unit of length and L/v as the unit of time. We use capital letters to denote the nondimensionalized parameters ($S = sL/v$ and so on). Then the equations become

$$\frac{\partial \rho_R}{\partial t} = \frac{\delta}{2}\frac{\partial^2 \rho_R}{\partial x^2} + (2\rho_R - 1)\frac{\partial \rho_R}{\partial x} + K_{\text{on}}c(1-\rho_R) - K_{\text{off}}\rho_R - S\rho_R + S\rho_L \tag{S5}$$

$$\frac{\partial \rho_L}{\partial t} = \frac{\delta}{2}\frac{\partial^2 \rho_L}{\partial x^2} + (1 - 2\rho_L)\frac{\partial \rho_L}{\partial x} + K_{\text{on}}c(1-\rho_L) - K_{\text{off}}\rho_L + S\rho_R - S\rho_L. \tag{S6}$$

We choose $x = 0$ as the center of the overlap, so the boundary conditions become $\rho_R(-0.5) = \rho_L(0.5) = \alpha$ and $\rho_R(0.5) = \rho_L(-0.5) = 1 - \beta$.

Because δ is small, we typically neglect the second derivative terms. However, if the first derivative terms are close to 0, which occurs when $\rho \approx 1/2$, the second-derivative terms may be important. The steady-state equations with second-derivative terms neglected are

$$0 = (2\rho_R - 1)\frac{\partial \rho_R}{\partial x} + K_{\text{on}}c(1-\rho_R) - K_{\text{off}}\rho_R - S\rho_R + S\rho_L, \tag{S7}$$

$$0 = (1 - 2\rho_L)\frac{\partial \rho_L}{\partial x} + K_{\text{on}}c(1-\rho_L) - K_{\text{off}}\rho_L + S\rho_R - S\rho_L. \tag{S8}$$

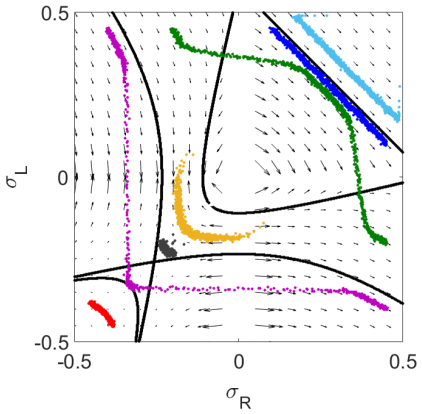

FIG. S3. The phase space flows for the simulations shown in figure 2 in the main text. The parameters used are the reference parameter set of table 1 with a bulk motor concentration of 200 nM, except for the switching rate which is 0.1 s^{-1} and the boundary conditions as noted below. H_n: high-density center-minimum phase ($\alpha = 0.95$, $\beta = 0.99$, light blue). H_x: high-density center-maximum phase ($\alpha = 0.6$, $\beta = 0.95$, dark blue). LH_x: low density-high density center-maximum coexistence ($\alpha = 0.3$, $\beta = 0.95$, green). M: Meissner phase $\alpha = 0.6$, $\beta = 0.4$, yellow). L_n: low-density center-minimum phase ($\alpha = 0.3$, $\beta = 0.4$, black). LH_n: low density-high density center-minimum coexistence ($\alpha = 0.1$, $\beta = 0.95$, magenta). L_x: low-density center-maximum phase ($\alpha = 0.05$, $\beta = 0.1$, red).

A. Exact solution

To find spatially varying solutions to Eqn. S7, S8, we first define $\sigma_{R,L} = \rho_{R,L} - \frac{1}{2}$ as the difference of the densities from 1/2. We also define a shorthand for the rate combinations $k = K_{on}c + K_{off} + S$ and $\gamma = K_{on}c - K_{off}$. Then the equations become

$$\frac{d\sigma_R}{dx} = \frac{k}{2} - \frac{\gamma}{4\sigma_R} - \frac{S\sigma_L}{2\sigma_R} \tag{S9}$$

$$\frac{d\sigma_L}{dx} = -\frac{k}{2} + \frac{\gamma}{4\sigma_L} + \frac{S\sigma_R}{2\sigma_L}. \tag{S10}$$

Eqns S9 and S10 are well defined for $\sigma_{R,L} \neq 0$. Next we introduce the sum and difference of the densities, the total motor concentration $\phi(x) = \sigma_R + \sigma_L$ and $\omega(x) = \sigma_R - \sigma_L$. The equations are

$$\frac{d\phi}{dx} = \frac{\gamma\omega + 2S\phi\omega}{\phi^2 - \omega^2}, \tag{S11}$$

$$\frac{d\omega}{dx} = \frac{(k-S)\phi^2 - \gamma\phi - (k+S)\omega^2}{\phi^2 - \omega^2}, \tag{S12}$$

which can be combined to give

$$\omega\frac{d\omega}{d\phi} = \frac{(k-S)\phi^2 - \gamma\phi - (k+S)\omega^2}{\gamma + 2S\phi}. \tag{S13}$$

Defining $\eta(\phi) = \omega^2(\phi)$, this can be rewritten

$$\frac{1}{2}\frac{d\eta}{d\phi} = \frac{(k-S)\phi^2 - \gamma\phi - (k+S)\eta}{\gamma + 2S\phi}, \tag{S14}$$

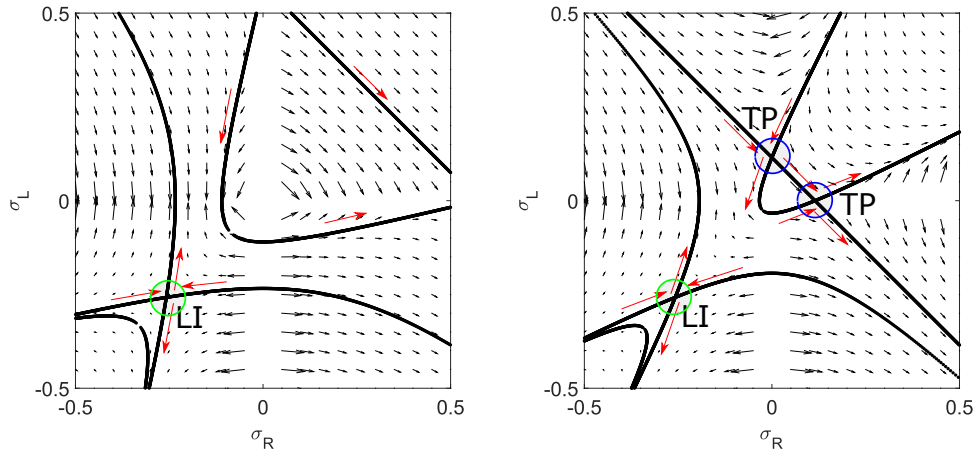

FIG. S4. Phase space flows. Left: low switching rate (0.1 s^{-1}); right, high switching rate (5 s^{-1}). Other parameters are the reference parameter set of table 1 with a bulk motor concentration of 200 nM, except the motor speed is 5 μm s^{-1}. The Langmuir isotherm is labeled LI, and the transition points are labeled TP.

or

$$\frac{\gamma + 2S\phi}{2} d\eta + [\gamma\phi - (k - S)\phi^2 + (k + S)\eta] d\phi = 0. \tag{S15}$$

This inexact ODE can be made exact through multiplication by the integrating factor $(\gamma+2S\phi)^{k/S}$. We then obtain the solution by direct integration,

$$C_1 = \int d\eta \; (\gamma + 2S\phi)^{k/S} \left[\frac{\gamma + 2S\phi}{2}\right] + \int d\phi \; (\gamma + 2S\phi)^{k/S} \left[\gamma\phi - (k - S)\phi^2 + (k + S)\eta\right], \tag{S16}$$

$$C_1 = \frac{\eta}{2}(\gamma + 2S\phi)^{1+k/S} - (\gamma + 2S\phi)^{1+k/S} \frac{\gamma^2 - 2(k + S)\gamma\phi + (k - S)(k + 2S)\phi^2}{2(k + 2S)(k + 3S)}, \tag{S17}$$

which gives the exact solution

$$\omega^2(\phi) = \frac{C}{(\gamma + 2S\phi)^{1+k/S}} - \frac{2(k + S)\gamma\phi - (k - S)(k + 2S)\phi^2 - \gamma^2}{(k + 2S)(k + 3S)}. \tag{S18}$$

Here C_1 and C denote integration constants.

This solution is the relationship between ω and ϕ that satisfies the steady-state equation. This is plotted as the black curves in the phase portraits of figs. S2 – S5. Note that for boundary conditions $\alpha = \beta = 0$, $\sigma_R(\mp 0.5) = \mp 0.5$ and $\sigma_L(\mp 0.5) = \pm 0.5$. Therefore, the filament ends correspond to the upper left and lower right corners in the phase portraits of fig. S2. Other boundary conditions correspond to other pointes in the phase plane. As expected, the direction of change of the exact solutions follow the phase arrows. In fig. S2, the linear and linear-log curves are approximations that hold near the overlap ends, as described below.

We overlaid the results of kMC simulations of the discrete model in red. From this representation, we can see how the phase-plane motor density is connected to the approximately linear variation of motor density: the boundary layers where the motor density is linearly increasing/decreasing show up as the sloped red lines near the upper left and lower right corners of the phase plane. The

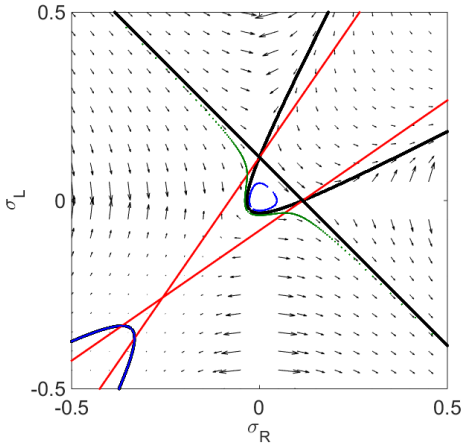

FIG. S5. Phase space flows showing curves adjacent to the the $C = 0$ curve. The green curve has C slightly greater than zero and is an open curve. The blue curve has C slightly less than zero and is a closed curve. The red lines are nullclines.

approximately constant density region in the center of the filaments corresponds to the set of points in the lower left of the phase plane, and the crossover between the boundary layers and the approximately constant region are the red horizontal and vertical lines.

Our simulation results (red) deviate substantially from the exact solutions to the continuum equations (black). In particular, near the overlap edges, the densities follow an exact solution with integration constant C_1, then cross over to an exact solution with integration constant C_2 for the overlap central region. This occurs because the exact solution we found to the continuum equations (Eqn. S18) does not satisfy the nonlocal total binding constraint (Eqn. 11).

III. PHASE DIAGRAM

Similar to the single-filament case [5], we find low density (L), high density (H), low density-high density (LH), and Meissner (M) phases. Low density is < 0.5, and high density > 0.5. Switching between the two antiparallel filaments causes the motor density to become either higher or lower at the center. In addition, for high switching rate a low density-high density-low density-high density (LHLH) phase appears. We describe the conditions for each phase to occur below assuming a rightward-oriented (R) filament, as in fig. 2 in the main text.

The motor density profile is determined by the phase space flow (fig. S3, S4). For low switching rate (fig. S4, left), there is only one fixed point, the Langmuir isotherm. However, once the switching rate becomes sufficiently high, a pair of transition points (TP) appear (fig. S4, right). The transition points are the intersections of the nullclines and the $\sigma = 0$ lines. We call the line which connects the two TP the transition line.

For a fixed overlap length, the total number of lattice sites is constant. Therefore the density profile must connect the starting and ending points with a number of steps equal to the number of sites. If this is not possible, one or both boundary conditions cannot be satisfied.

Symbol	Parameter	Large-S value	Notes
v	Motor speed	0.5 μm s^{-1}	Same as reference parameters
k_{on}	Binding rate constant	2.7×10^{-6} nM^{-1} s^{-1}	Reduced by 10^2 for large-S parameters
c	Bulk motor concentration	1–200 nM	Same as reference parameters
k_{off}	Unbinding frequency	1.69×10^{-3} s^{-1}	Reduced by 10^2 for large-S parameters
s	Switching rate	0.44 s^{-1}	Same as reference parameters
α	Motor flux constant into overlap from MT minus end	0	Same as reference parameters
β	Motor unbinding rate constant from MT plus end	0	Same as reference parameters
N	Number of sites	120-2500	Same as reference parameters
δ	Length of a single site	8 nm	Same as reference parameters

TABLE S1. Model parameters for large-S parameter set. We reduced the binding and unbinding rates by a factor of 10^2 relative to the reference parameters (table 1 in the main text).

1. Low density

The low-density phase occurs when $\alpha < 0.5$ and the right boundary condition cannot be satisfied. If $\alpha < \rho_0$, the motor density profile has a local maximum at the center. If $\alpha > \rho_0$, the motor density profile has a local minimum at the center.

2. Low density-high density

The domain wall occurs where the density changes from L to H. This means the profile crosses the $\sigma = 0$ ($\rho = 1/2$) line. The matching condition between L and H phases is continuity in the current [5] $\rho(x_l) = 1 - \rho(x_r)$ or $\sigma(x_l) = -\sigma(x_r)$. We determine the domain wall position using the symmetry of the total motor density in the overlap, which means that the center density must lie on the $\alpha = 1 - \beta$ line. By computing the density profile from $x = 0$ to $x = -0.5$ or 0.5, we can identify when the domain walls occur at $x_w = -0.5$ or 0.5 lines. If the domain wall position is greater than 0, the overall microtubule overlap shows higher density at the center rather than at the boundaries.

3. High density

The high-density phase occurs when $\alpha > 0.5$ and the left boundary condition cannot be satisfied. The transition density ρ_t separates the center-maximum and center-minimum density profiles, determined by the value of ρ_L when the transition line intercepts the $x_w = 0.5$ line. If $1 - \beta < \rho_t$, density profile has a local maximum at the center; while $1 - \beta > \rho_t$, the motor density profile has a local minimum at the center.

4. Meissner

The Meissner phase occurs when $\alpha > 0.5$ and $1 - \beta < 0.5$. Both boundary conditions cannot be fulfilled, so the density profile is independent of the boundary conditions.

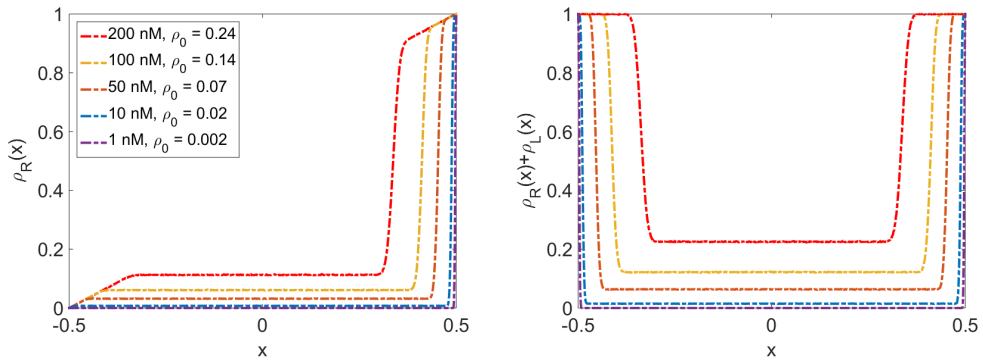

FIG. S6. Motor density profiles for the large-S parameter set. Left: motor density $\rho_R(x)$ on MT with rightward-moving motors. Right: total motor density $\rho_R(x) + \rho_L(x)$ on both MTs in the overlap.

5. *Low density-high density-low density-high density*

The LHLH phase with multiple domain walls occurs when $\alpha < 0.5$ and the switching rate is sufficiently high (fig. 2). The transition points occur where the $C = 0$ analytic solution (equation S18) intersects the transition lines. This makes the flows (fig. S5, blue curve) bounded if the profile is closer to the $\sigma_R = 0$ curve. Thus, the region between the domain wall curves and $\sigma_R = 0$ line is the place where the profiles are bounded which need not only one domain wall but three domain walls in order to connect to the end point.

IV. LARGE SWITCHING RATE PARAMETER SET RESULTS

In fig. S6 we show the motor density profiles for the large-S parameter set.

V. EFFECTS OF THE TOTAL BINDING CONSTRAINT

A. Linear solution near overlap ends

Near the ends of the overlap, the variation of density becomes approximately linear. Consider the left end of the overlap near $x = -1/2$, where $\rho_R \approx 0$ and $\rho_L \approx 1$. This implies that $\sigma_R \approx -1/2$ and $\sigma_L \approx 1/2$, so $\sigma_R \approx -\sigma_L$. Then equations S9 and S10 become approximately

$$\frac{d\sigma_R}{dx} = K_{\text{on}}c + S \tag{S19}$$

$$\frac{d\sigma_L}{dx} = -(K_{\text{off}} + S). \tag{S20}$$

Therefore, near the overlap ends the motor density varies linearly. We can achieve a better approximation to the motor density near the overlap ends by including the density dependence of the

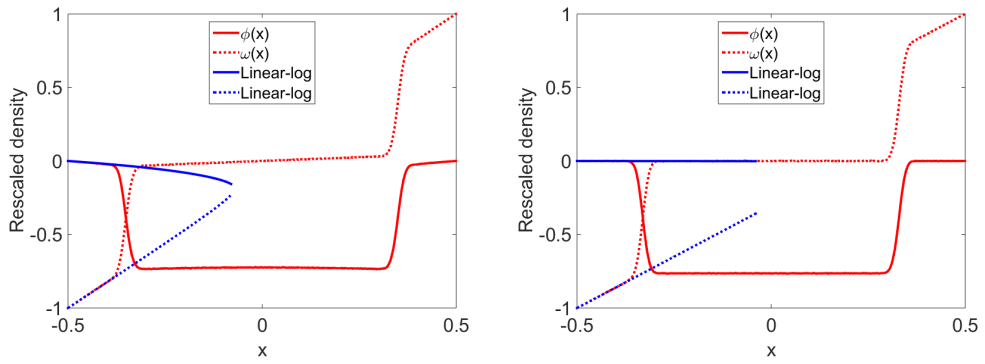

FIG. S7. Comparison of simulation results with approximate solutions valid near overlap ends. Left: experimental parameter set; right: large-S parameter set; both use a bulk motor concentration of 200 nM. Red curves are simulation results, blue curves are approximate solutions valid near the ends of the overlap.

term inversely proportional to density. Then the approximate equations are

$$\frac{d\sigma_R}{dx} = \frac{k+S}{2} - \frac{\gamma}{2\sigma_R} \tag{S21}$$

$$\frac{d\sigma_L}{dx} = -\frac{k+S}{2} + \frac{\gamma}{2\sigma_L}. \tag{S22}$$

An implicit solution for the densities as a function of x is

$$x - x_0 = \frac{2\sigma_R(k+S) + \gamma\log(\gamma - 2(k+S)\sigma_R)}{(k+S)^2} \tag{S23}$$

$$x - x_0 = -\frac{2\sigma_L(k+S) + \gamma\log(\gamma - 2(k+S)\sigma_L)}{(k+S)^2}. \tag{S24}$$

We plot these approximate solutions on the phase plane in fig. S2 and superimposed on the density profiles in fig. S7. As expected, the approximations agree well with simulation results near the overlap ends.

B. Total binding constraint

Motor density profiles must satisfy the total binding constraint of Eqn. 11. We verified that the total binding constraint is satisfied in our simulations by determining the integrated motor density and comparing it to ρ_0 (fig. S8). Whether we vary the bulk motor concentration or the motor speed, we find good agreement between simulations and theory, verifying that Eqn. 11 is satisfied in our model.

To derive an analytic approximation for the motor density, overlap central density, and boundary layer length, we assume the motor densities vary linearly near the filament ends (equations S19 and S20), and that the domain walls are infinitely thin so that we can neglect them in integrating the density. A filament can be divided it into three regions separated by the symmetric boundary

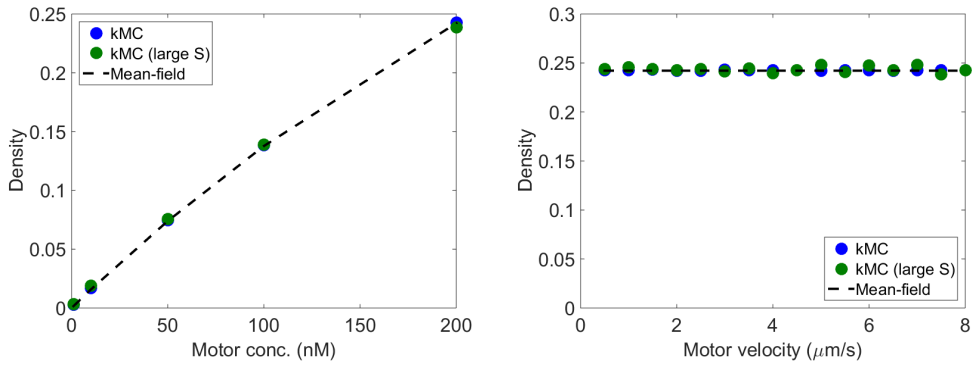

FIG. S8. Total binding constraint. Points show the integral of the motor density on a single filament as described by Eqn. 11. The dashed line is ρ_0. For all simulations performed, the total binding constraint is satisfied.

layer ends are $\pm x_{\rm bl}$ (fig. S9). The density is approximately

$$\rho_R(x) = \begin{cases} (K_{\rm on}c + S)(x + \frac{1}{2}) & -\frac{1}{2} \le x \le -x_{\rm bl} \\ \rho_0 + A\cosh\lambda x + B\sinh\lambda x & -x_{\rm bl} \le x \le x_{\rm bl} \\ (K_{\rm off} + S)(x - \frac{1}{2}) + 1 & x_{\rm bl} \le x \le \frac{1}{2} \end{cases} \tag{S25}$$

The middle formula in equation S25 is the solution of equations 9 and 10 if we neglect the nonlinear terms, which is a good approximation since the the density profile doesn't change much with position in the central region. The constant λ is defined by $\lambda^2 = (K_{\rm on}c + K_{\rm off} + 2S)(K_{\rm on}c + K_{\rm off})$ and ρ_0 is the Langmuir density. The coefficients A and B are derived by using continuity in the density at left end, $(K_{\rm on}c + S)(\frac{1}{2} - x_{\rm bl})$, and continuity in the flux at the right end, $1 - ((K_{\rm off} + S)(x_{\rm bl} - \frac{1}{2}) + 1) = (K_{\rm off} + S)(\frac{1}{2} - x_{\rm bl})$. Then we find

$$A = \frac{(\frac{1}{2} - x_{\rm bl})(K_{\rm on}c + K_{\rm off} + 2S) - 2\rho_0}{2\cosh(\lambda x_{\rm bl})} \tag{S26}$$

$$B = \frac{(\frac{1}{2} - x_{\rm bl})(K_{\rm off} - K_{\rm on}c)}{2\sinh(\lambda x_{\rm bl})} \tag{S27}$$

For the reference parameter set that we study here, the motor speed is large compared to the other rates, making the dimensionless rates small and therefore $\lambda x \ll 1$. We can then approximate $\cosh(\lambda x) \approx 1$ and $\sinh(\lambda x) \approx \lambda x$.

We then find the approximate form of the density profile

$$\rho_R(x) = \begin{cases} (K_{\rm on}c + S)\left(x + \frac{1}{2}\right) & -\frac{1}{2} \le x \le -x_{\rm bl} \\ \frac{x}{2x_{\rm bl}}\left(\frac{1}{2} - x_{\rm bl}\right)(K_{\rm off} - K_{\rm on}c) + \frac{1}{2}\left(\frac{1}{2} - x_{\rm bl}\right)(K_{\rm on}c + K_{\rm off} + 2S) & -x_{\rm bl} \le x \le x_{\rm bl} \\ (K_{\rm off} + S)\left(x - \frac{1}{2}\right) + 1 & x_{\rm bl} \le x \le \frac{1}{2} \end{cases} \tag{S28}$$

Plugging this approximation to the density into the total binding constraint (Eqn. 11), we find

$$-\frac{1}{8}(2x_{\rm bl} - 1)(4 + K_{\rm off}(6x_{\rm bl} - 1) + K_{\rm on}c(2x_{\rm bl} + 1) + 8Sx_{\rm bl}) = \rho_0, \tag{S29}$$

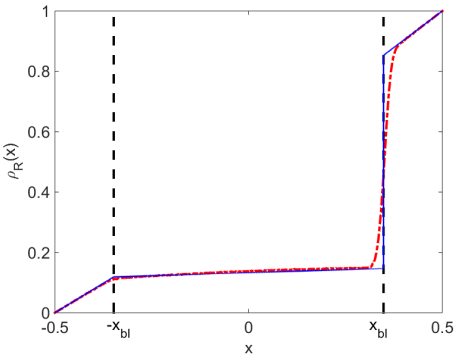

FIG. S9. Motor occupancy and boundary layer ends. Motor density profile $\rho_R(x)$ for rightward-moving motors. Red: kMC simulation results; blue: the linear approximation of Eqn. S28. The ends of the boundary layers are labeled $\pm x_{\rm bl}$. This simulation used the reference parameter set with bulk concentration $c = 200$ nM.

or

$$x_{\rm bl} = \frac{2(S + K_{\rm off} - 1) \pm \sqrt{4(1 - K_{\rm off} - S)^2 + (3K_{\rm off} + K_{\rm on}c + 4S)(4 - 8\rho_0 - K_{\rm off} + K_{\rm on}c)}}{2(3K_{\rm off} + K_{\rm on}c + 4S)}. \quad \text{(S30)}$$

The motor density in the center of the overlap is then

$$\rho_c = \frac{(1 - 2x_{\rm bl})(K_{\rm on}c + K_{\rm off} + 2S)}{4} \quad \text{(S31)}$$

This result shows that the motor density at the center of the overlap is not simply ρ_0, even when the overlap is long. Instead the center density depends on the motor speed and filament switching rate in addition to binding parameters. In fig. S9 we show the comparison of the approximate density profile and positions of the ends of the boundary layers. In fig. S10 we compare the analytic predictions for the boundary layer length to results from simulations.

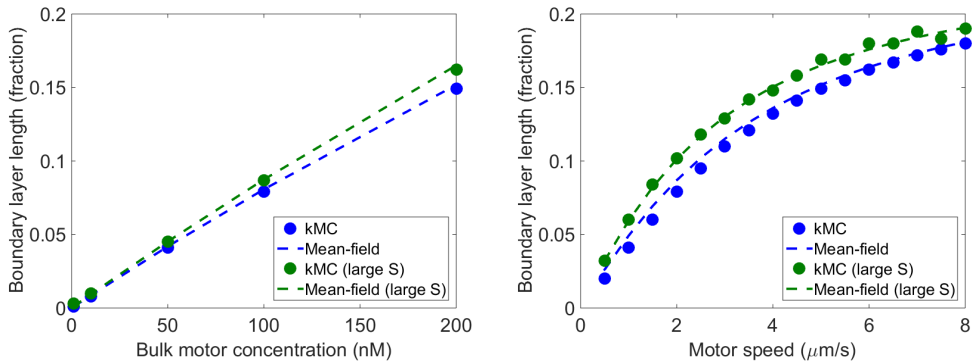

FIG. S10. Length of boundary layer overlap ends where motors accumulate, as a fraction of the total overlap length. Left: variation with bulk motor concentration; right: variation with motor speed. Points indicate simulation results and dashed lines predictions from Eqn. S30.